

Disturbance Observer based Constrained Resonant Control of SRM Integrated EV Drive in Vehicle-to-Home (V2H) Operation

Junaid Saeed*, Liuping Wang* and Nuwantha Fernando*

* Royal Melbourne Institute of Technology (RMIT) Melbourne 3000, Australia. (e-mail: junaid.saeed@rmit.edu.au).

Abstract: This paper presents a disturbance observer based constrained resonant control strategy for a switched reluctance motor (SRM) integrated electric vehicle (EV) drive in vehicle-to-home (V2H) mode of operation. First, a full-order large-signal model of the integrated drive is developed using averaged modeling technique. Then, a fixed switching frequency disturbance estimation based constrained resonant control with an intrinsic anti-windup mechanism is proposed to achieve a 50Hz sinusoidal voltage at the inverter output. It is shown through simulation studies that the proposed control scheme achieves excellent reference tracking and disturbance rejection with different linear and non-linear load types.

Keywords: Disturbance Observer, Resonant, Electric Vehicle, EV, Vehicle-to-Home, V2H, Integrated Drive, SRM

1. INTRODUCTION

Electric vehicles are emerging as an attractive means of transportation due to their long-term sustainability and low environmental impact in terms of carbon footprint (Gan et al., 2016; Romo and Micheloud, 2015). To this end, there are several ways that an EV can contribute towards a greener environment, such as grid power utilization enhancement, power quality improvement and ancillary services to facilitate large-scale integration of the renewable energy sources (Rassaei et al., 2015; Yan et al., 2019). The former is, for example, achieved by shifting the charging times of the EV batteries to attain demand response targets. The stored energy is then supplied to the grid in peak hours for remunerative gains. Similarly, EVs contribute to power quality improvement by supplying harmonic content to non-linear loads hence drawing only fundamental harmonic current from the grid.

With AC power supplying capability of the EV, the integrated EV drive can also power home appliances with a fixed 50/60Hz AC voltage in absence of the AC power grid. This mode is known as vehicle-to-home (V2H) mode (Robledo et al., 2018). In this mode, the EV drive can act as a standalone inverter, or can be configured to form an islanded nano-grid in presence of other participating electric vehicles (e.g. for an office or building) with active frequency control (Hu et al., 2015).

Owing to the complexity of different operating modes, the integrated EV drives make an interesting and challenging application in terms of the control design, and also require special attention with regards to the modelling. This paper presents a comprehensive modelling and control approach for the standalone V2H operation of a switched reluctance motor integrated drive (Hu et al., 2015). The specific contributions of this paper are: (i) development of an

averaged model for the integrated EV drive in standalone V2H mode, and (ii) development of a fixed switching frequency, disturbance observer based constrained resonant control strategy with anti-windup mechanism to produce a 50Hz sinusoidal voltage on the output in presence of unmeasured system disturbances. The effectiveness of the proposed control scheme has been verified using a number of test-scenarios including multiple linear and non-linear load types. Simulations have been performed in MATLAB/Simulink and several results have been included.

2. DESCRIPTION OF THE SRM INTEGRATED EV DRIVE

2.1 Circuit Configuration

The circuit diagram of the considered integrated EV drive (Saeed et al., 2019) is shown in Fig. 1(a) with its corresponding SR motor depicted in Fig. 1(b). The considered 6/4 SRM has three-phases, namely, a , b and c . Each phase consists of two windings, denoted with $L_{1\gamma}$ and $L_{2\gamma}$, respectively, and is powered by an asymmetric half-bridge (AHB) circuit (Sun et al., 2019). The respective AHB of each phase consists of two MOSFETs $S_{\gamma u}$ and $S_{\gamma d}$, and two diodes $D_{\gamma u}$ and $D_{\gamma d}$, where $\gamma \in \{a, b, c\}$. The drive is powered by a battery, B with its terminal voltage v_B . The battery voltage is stepped-up to feed power to the DC-link with the help of a bidirectional DC-DC converter. This DC-DC converter consists of two MOSFETs S_1 and S_2 and an inductor in series with the battery with inductance L and resistance R_L . The DC-link capacitor is denoted by C and its terminal voltage by v_{dc} . The AC load is connected across the middle-points of phase b and c windings through a mode selective relay. The capacitor at the load side is given by C_o with its voltage and current being v_o and i_c , respectively. The current through the output AC load is given by i_o . Moreover, in the V2H

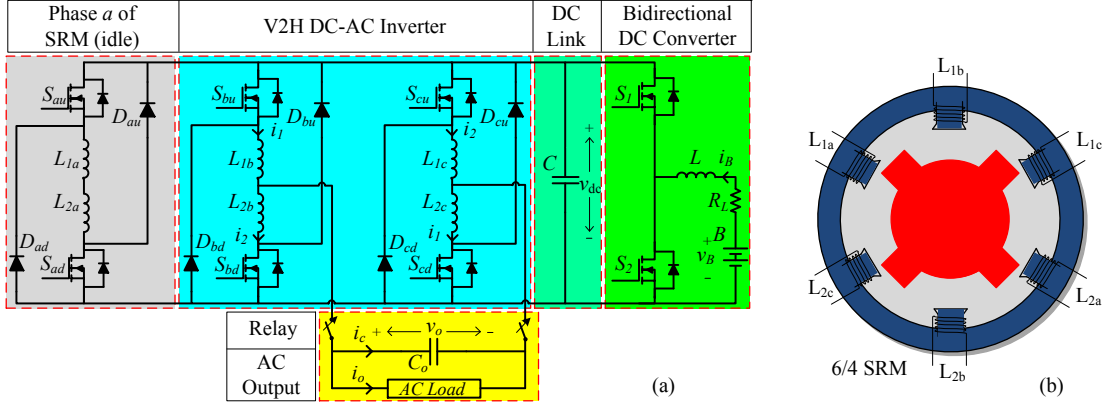


Fig. 1. (a) Circuit diagram of SRM integrated EV drive, and (b) 6 stator pole, 4 rotor pole switched reluctance motor.

mode, the current of L_{1b} and L_{1c} is denoted as i_1 and i_2 , respectively.

2.2 Operation in Standalone V2H Mode

In the V2H mode, the AHB circuits associated with the phases b and c constitute a DC-AC inverter. Since only two AHBs are required to achieve the single-phase inverter operation, the phase a AHB remains idle. The battery voltage is stepped-up to an appropriate voltage level and it is assumed that the DC-link voltage is regulated with the help of an appropriate control mechanism. The switches of the inverter are operated with sinusoidal pulse width modulation (SPWM) signals. The upper switch of one AHB is paired with the lower switch of the other AHB, i.e. S_{bu} and S_{cd} form one pair and are controlled with the same PWM signal. Similarly, S_{bd} and S_{cu} form the other pair, controlled with another PWM signal.

Fig. 2 shows the flow of current in V2H mode of the integrated SR drive. The highlighted red and blue portions indicate the flow of current in charging and discharging of the inductors, respectively. Moreover, for the convenience of analysis, it is assumed that the DC-link voltage is fairly constant and is replaced with a DC voltage source which is capable to supply and absorb electrical power. Furthermore, it is also assumed that the circuit is in steady-state operation with all the inductors and capacitors carrying their respective residual charge from the previous switching cycle. Fig. 2(a) shows the current flow when S_{bu}/S_{cd} are in conduction and S_{bd}/S_{cu} are in blocking state. In this instance, the inductors L_{1b} and L_{2c} are charging from the DC-link and the current i_1 is increasing. On the other hand, the current i_2 (L_{1c} and L_{2b}) is decreasing as it is freewheeling through the diodes D_{bu} and D_{cd} . The current i_2 is feeding energy back to the DC-link and its path is shown with blue dashed arrow in Fig. 2(a).

Similarly, Fig. 2(b) illustrates the flow of current when S_{bd}/S_{cu} are ON and S_{bu}/S_{cd} are in OFF state. In this instance, the current i_2 builds up in L_{p2} and the already established i_1 freewheels through D_{bd} and D_{cu} to charge the DC-link. The average current in one switching cycle depends on the type of AC load connected and the phase difference between the load quantities, v_o and i_o . It is however, worthwhile to mention that in a complete AC cycle, the current i_1 and i_2 remain unidirectional.

3. LARGE-SIGNAL AVERAGED MODELLING OF THE INTEGRATED EV DRIVE

Large-signal averaged models are extensively employed for the control design of power electronic converters (Bayat et al., 2018; Sun et al., 2001). The dynamic model of the circuit is developed in different switch modes and the resulting models are added as a weighted sum of the control input to acquire the averaged model. In the following subsections, the time interval of one switching cycle has been taken as T_s , and the time interval for which the switches S_{bu}/S_{cd} are conducting, is denoted by dT_s , where d is the duty cycle of the converter such that $d \in [0, 1]$. Moreover, the output load of the circuit has been assumed purely resistive in order to avoid imaginary terms in the physical model.

3.1 Dynamic Equations for $t = 0$ to dT_s

Fig. 2(a) shows the current flow of the SR drive when S_{bu}/S_{cd} are ON and S_{bd}/S_{cu} are OFF. In this mode, the current i_1 (shown in red) is rising and the voltage drop across the inductor L_{1b} is given by,

$$v_{L_{1b}} = v_{dc} - v_o - v_{L_{2c}} \quad (1)$$

where $v_{L_{1b}}$ and $v_{L_{2c}}$ are the voltages across L_{1b} and L_{2c} , respectively. Since L_{1b} and L_{2c} are essentially in series, they can be combined into one inductance L_{p1} such that $L_{p1} = L_{1b} + L_{2c}$. Considering this, (1) can be written as

$$v_{L_{1b}} + v_{L_{2c}} = v_{dc} - v_o \quad (2)$$

$$\implies \frac{di_1}{dt} = \frac{v_{dc}}{L_{p1}} - \frac{v_o}{L_{p1}} \quad (3)$$

Similarly, the current i_2 (shown in blue) through $L_{2b} + L_{1c}$ being opposite to i_1 , is feeding the energy back to the DC-link. In this case, the voltage drop across the respective inductors is given by

$$v_{L_{1c}} + v_{L_{2b}} = -v_{dc} + v_o \quad (4)$$

$$\implies \frac{di_2}{dt} = -\frac{v_{dc}}{L_{p2}} + \frac{v_o}{L_{p2}} \quad (5)$$

where $v_{L_{1c}}$ and $v_{L_{2b}}$ are the voltage drops across L_{2b} and L_{1c} , respectively, and $L_{p2} = L_{1c} + L_{2b}$.

The instantaneous current of the output capacitor C_o can be obtained by applying KCL at the output node and is given as

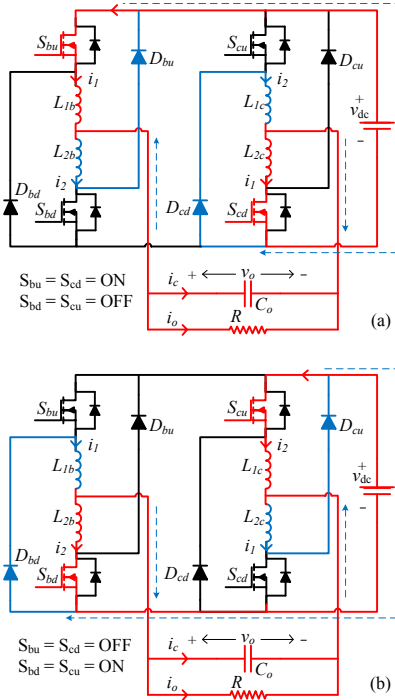


Fig. 2. Flow of current through the integrated EV drive - (a) $t = 0 \rightarrow dT_s$, and (b) $t = dT_s \rightarrow T_s$.

$$i_c = i_1 - i_2 - i_o \quad (6)$$

$$\Rightarrow \frac{dv_o}{dt} = \frac{i_1}{C_o} - \frac{i_2}{C_o} - \frac{v_o}{RC_o} \quad (7)$$

where R is the load resistance. The dynamic state-space model of the integrated drive in this interval can be written as

$$\begin{cases} \dot{x} = A_1 x + B_1 v_{dc} \\ y = C_1 x \end{cases} \quad (8)$$

where,

$$A_1 = \begin{bmatrix} 0 & 0 & -\frac{1}{L_{p1}} \\ 0 & 0 & \frac{1}{L_{p2}} \\ \frac{1}{C_o} & -\frac{1}{C_o} & -\frac{1}{RC_o} \end{bmatrix}, B_1 = \begin{bmatrix} \frac{1}{L_{p1}} \\ -\frac{1}{L_{p2}} \\ 0 \end{bmatrix} \quad (9)$$

$$x = [i_1 \ i_2 \ v_o]^T, C_1 = [0 \ 0 \ 1].$$

Here, A_1 , B_1 and C_1 are system, input and output matrices, respectively. Furthermore, x and y denote the state and output vectors of the system, respectively.

3.2 Dynamic Equations for $t = dT_s$ to T_s

The current flow of the integrated drive from dT_s to T_s is depicted in Fig. 2(b). Here, the current i_1 (shown in blue) is decreasing, supplying power to the AC output capacitor. In this case, the current dynamics are given by

$$v_{L_{1b}} + v_{L_{2c}} = -v_{dc} - v_o \quad (10)$$

$$\Rightarrow \frac{di_1}{dt} = -\frac{v_{dc}}{L_{p1}} - \frac{v_o}{L_{p1}} \quad (11)$$

Similarly, i_2 (shown in red) is increasing under the effect of v_{dc} and v_o with its dynamics given as

$$\frac{di_2}{dt} = \frac{v_{dc}}{L_{p2}} + \frac{v_o}{L_{p2}} \quad (12)$$

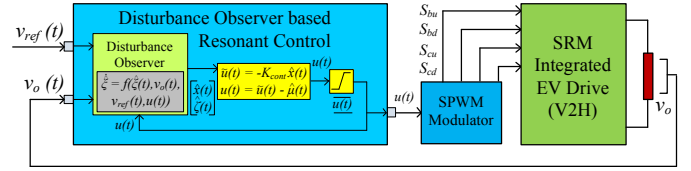


Fig. 3. Block diagram of the system with the disturbance observer based control mechanism; $\hat{\xi} = [\hat{x}(t)^T \ \hat{\zeta}(t)^T]^T$.

Moreover, it is worthwhile to note that C_o is still charging under the effect of $i_1 - i_2 - i_o$. Therefore, the output voltage dynamics remains unchanged and is given as (7). In this interval, the resulting state-space model is given by

$$\begin{cases} \dot{x} = A_2 x + B_2 v_{dc} \\ y = C_2 x \end{cases} \quad (13)$$

where,

$$A_2 = \begin{bmatrix} 0 & 0 & -\frac{1}{L_{p1}} \\ 0 & 0 & \frac{1}{L_{p2}} \\ \frac{1}{C_o} & -\frac{1}{C_o} & -\frac{1}{RC_o} \end{bmatrix}, B_2 = \begin{bmatrix} -\frac{1}{L_{p1}} \\ \frac{1}{L_{p2}} \\ 0 \end{bmatrix} \quad (14)$$

$$x = [i_1 \ i_2 \ v_o]^T, C_2 = [0 \ 0 \ 1]$$

3.3 Averaged Model of the Integrated Drive

The averaged state-space model of the integrated drive is obtained by combining (8) and (13) as a weighted sum of the duty cycle d . The resulting averaged state-space model is given as

$$\begin{cases} \dot{x} = A_p x + \tilde{B}_p v_{dc} \\ y = C_p x \end{cases} \quad (15)$$

where,

$$A_p = dA_1 + (1-d)A_2 = \begin{bmatrix} 0 & 0 & -\frac{1}{L_{p1}} \\ 0 & 0 & \frac{1}{L_{p2}} \\ \frac{1}{C_o} & -\frac{1}{C_o} & -\frac{1}{RC_o} \end{bmatrix} \quad (16)$$

$$\tilde{B}_p = dB_1 + (1-d)B_2 = \begin{bmatrix} \frac{2d-1}{L_{p1}} & \frac{1-2d}{L_{p2}} & 0 \end{bmatrix}^T \quad (17)$$

$$C_p = dC_1 + (1-d)C_2 = [0 \ 0 \ 1] \quad (18)$$

The averaged input matrix \tilde{B}_p is a function of the control input d . Here, a change of variable has been introduced to simplify the model given by (15) and the resulting model is given in terms of the new control variable $u(t)$,

$$\dot{x}(t) = A_p x(t) + B_p u(t) \quad (19)$$

where

$$u(t) = 2d(t) - 1 \quad (20)$$

and the matrix B is given as

$$B_p = \begin{bmatrix} \frac{v_{dc}}{L_{p1}} & -\frac{v_{dc}}{L_{p2}} & 0 \end{bmatrix}^T \quad (21)$$

It is worthwhile to note that the new control variable $u(t)$ will have its limits as $[-1, 1]$ unlike $d(t)$ which was limited between 0 and 1.

4. DISTURBANCE OBSERVER BASED CONSTRAINED RESONANT CONTROL

In this application, the control objective is to produce a fixed frequency 50Hz sinusoidal voltage across the output capacitor C_o in the presence of operational constraints of

the control input. The reference signal $v_{ref}(t)$ is generated by

$$v_{ref}(t) = V_m \sin(100\pi t) \quad (22)$$

where V_m is the peak amplitude of the sinusoid. The block diagram of the proposed disturbance observer based control structure is shown in Fig. 3.

4.1 Control Design

Since the output load appears as an unmeasured disturbance in the system, a mitigation mechanism needs to be in place for tight regulation of the output voltage in presence of load disturbances. For this purpose, the existence of a sinusoidal disturbance $\mu(t)$ in the control signal has been assumed such that

$$\begin{aligned} \dot{x}(t) &= A_p x(t) + B_p (u(t) + \mu(t)), \\ y(t) &= C_p x(t). \end{aligned} \quad (23)$$

where

$$\mu(t) = \mu_m \sin(100\pi t + \psi_0). \quad (24)$$

Here μ_m and ψ_0 represent the amplitude and phase of the disturbance, respectively. This input disturbance is represented in canonical state-space form as

$$\dot{\zeta} = A_\mu \zeta \quad (25)$$

where

$$A_\mu = \begin{bmatrix} 0 & -(100\pi)^2 \\ 1 & 0 \end{bmatrix}, \quad \zeta = \begin{bmatrix} \dot{\mu}(t) \\ \mu(t) \end{bmatrix}. \quad (26)$$

In this application, it has been assumed that the output voltage v_o (i.e. the system output) is the only measured variable. Hence, the state vector along with the periodic input disturbance needs to be estimated. For this purpose, the model of the system has been modified by augmenting the disturbance into the state vector. The resulting system is given by

$$\begin{aligned} \begin{bmatrix} \dot{x}(t) \\ \dot{\zeta}(t) \end{bmatrix} &= \begin{bmatrix} A_p & \bar{B}_p \\ O_{2 \times 3} & A_\mu \end{bmatrix} \begin{bmatrix} x(t) \\ \zeta(t) \end{bmatrix} + \begin{bmatrix} B_p \\ O_{2 \times 1} \end{bmatrix} u(t) \\ y(t) &= [C_p \ O_{1 \times 2}] \begin{bmatrix} x(t) \\ \zeta(t) \end{bmatrix}. \end{aligned} \quad (27)$$

where $\bar{B}_p = [O_{3 \times 1} \ B_p]$, and $O_{m \times n}$ represents a zero matrix of order $m \times n$.

Furthermore, it can be shown that if the original pair of system matrices A_p, C_p is observable, the augmented system in (27) is also observable (Wang, 2019). In this case, the original model (15) is observable. Hence, an observer can be designed to estimate the state and the disturbance vectors. With $\hat{x}(t)$ and $\hat{\zeta}(t)$ being the estimates of the state vector and the disturbance vector, respectively, the full-order system observer is given by

$$\begin{aligned} \begin{bmatrix} \dot{\hat{x}}(t) \\ \dot{\hat{\zeta}}(t) \end{bmatrix} &= \begin{bmatrix} A_p & \bar{B}_p \\ O_{2 \times 3} & A_\mu \end{bmatrix} \begin{bmatrix} \hat{x}(t) \\ \hat{\zeta}(t) \end{bmatrix} + \begin{bmatrix} B_p \\ O_{2 \times 1} \end{bmatrix} u(t) \\ &+ K_{obs} (v_o(t) - v_{ref}(t) - [C_p \ O_{1 \times 2}] \begin{bmatrix} \hat{x}(t) \\ \hat{\zeta}(t) \end{bmatrix}) \end{aligned} \quad (28)$$

where K_{obs} is the observer gain which has been chosen to achieve the observer error system stability and the desired dynamic performance.

It is important to note that the disturbance model augmentation embeds uncontrollable modes into the augmented system of (27), which renders it uncontrollable.

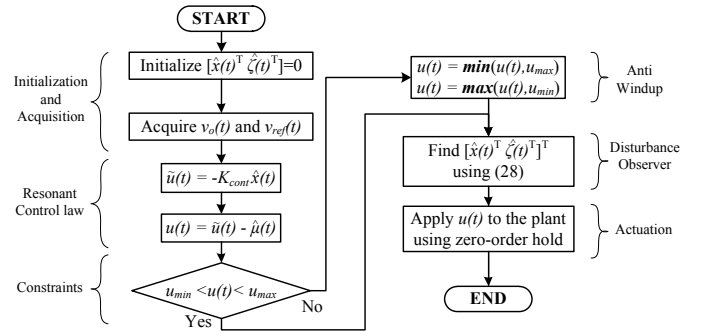


Fig. 4. Flowchart of the disturbance observer based control algorithm with anti-windup.

Table 1. Parameters of SRM Integrated Drive

Parameter Name	Symbol	Value
Battery Voltage	v_B	200V
Battery Series Inductance	L	0.5mH
Battery Series Resistance	R	0.2Ω
Nominal DC-link Voltage	v_{dc}	400V
Desired Peak Output Voltage	V_m	339.6V
Desired Output Voltage Frequency	f	50Hz
SRM Winding Inductance	L_{p1}	11.5mH
SRM Winding Inductance	L_{p2}	11.5mH
DC-link Capacitor	C	1000μF
AC Output Capacitor	C_o	20μF
Switching Frequency	$f_s = 1/T_s$	20kHz

Therefore, a controller has been designed for the original system of (23). The resulting state-feedback control law is given as

$$\tilde{u}(t) = -K_{cont} x(t) \quad (29)$$

where $\tilde{u}(t) = u(t) + \mu(t)$. Moreover, K_{cont} is the controller gain, which has been chosen to yield the closed-loop eigenvalues of the system in the left half of the s -plane and the desired closed-loop performance characteristics.

With the estimates of state and disturbance vectors available from (28), the resulting resonant control law is given as

$$u(t) = -K_{cont} \hat{x}(t) - \hat{\mu}(t) \quad (30)$$

where $\hat{\mu}(t) = [0 \ 1] \hat{\zeta}(t)$.

4.2 Constraints and Anti-Windup Mechanism

As discussed in Section-3, the control signal $u(t)$ has to fulfil the operational constraints of the system such that

$$-1 \leq u(t) \leq 1. \quad (31)$$

An important aspect of the proposed control structure is that because of the system implementation with the disturbance observer, which is a stable system, the anti-windup mechanism naturally occurs when the control signal is saturated. Fig. 4 shows the flowchart of the proposed control scheme. At the start, the estimates $\hat{x}(t)$ and $\hat{\zeta}(t)$ are initialized as zero. Then, at each time step, the output voltage $v_o(t)$ is measured from the plant. Based on the estimated state and disturbance vectors, the controller calculates the control input according to (30). The resulting control signal, however, is not necessarily bounded between $[-1, 1]$. Therefore, the control signal

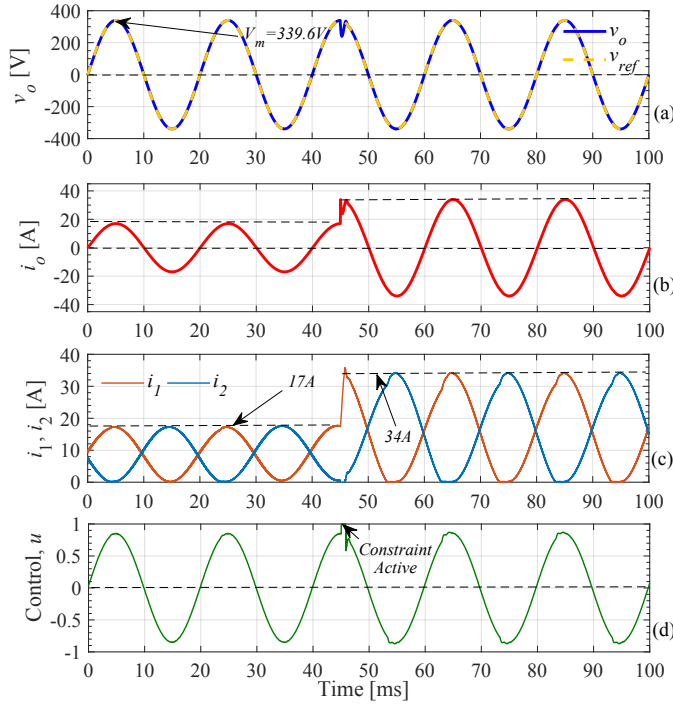


Fig. 5. Waveforms of standalone V2H mode with the proposed control with resistive load. (a) Output voltage v_o . (b) Output current i_o . (c) Inductor currents, i_1 and i_2 . (d) Control input u .

is constrained according to (31). Then, the observer is updated based on the constrained $u(t)$. After the observer update, the plant is actuated using a zero-order hold, and the whole process is repeated after the acquisition of next sampled data.

It is worthwhile to note that the disturbance observer is implemented after the control signal has been constrained. This results in a natural emulation of the anti-windup structure in case of the input saturation since the updated estimates $\hat{x}(t)$ and $\hat{z}(t)$ are based on a constrained value of the control input rather than what resulted from (30).

5. RESULTS

In order to assess the performance of the proposed disturbance observer control scheme for standalone V2H mode operation, a virtual hardware of the SRM integrated EV drive has been constructed in MATLAB/Simulink using the parameters mentioned in Table-1. The peak amplitude of the desired sinusoidal voltage has been selected as $\sqrt{2} \times 240V = 339.6V$ and the switching frequency of the converter is chosen to be $20kHz$. A number of test scenarios with multiple linear and non-linear output load types have been performed and are presented here.

5.1 Resistive Load

The waveforms for the operation of the integrated drive with the proposed control scheme in case of pure resistive load of 20Ω are shown in Fig. 5. Fig. 5(a) and 5(b) depict the voltage and current waveforms, respectively. It can be seen that the voltage waveform is successfully tracking its reference given by (22), and the output current i_o is

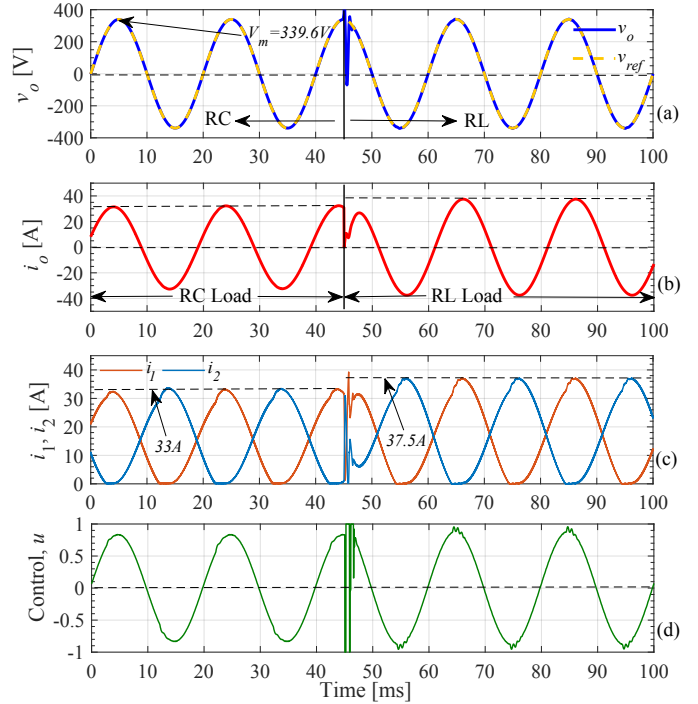


Fig. 6. Waveforms of standalone V2H mode with the proposed control with RC and RL load. (a) Output voltage v_o . (b) Output current i_o . (c) Inductor currents, i_1 and i_2 . (d) Control input u .

in phase with the voltage. Fig. 5(c) shows the inductor currents i_1 and i_2 in brown and blue colors, respectively. It is interesting to note that the output current i_o is essentially equal to $i_1 - i_2$ less the switching ripple. This can be readily verified by matching the peaks of the load current with those of i_1 and i_2 , which occur at $17A$ prior to $t = 45ms$. At $t = 45ms$, the output resistance is reduced from 20Ω to 10Ω , increasing the load two-fold. It can be seen in Fig. 5(d) that in order to compensate the drop in the output voltage due to load change, the constraint of upper control bound becomes active as $u = 1$. Eventually, the output voltage comes back to its desired reference after completely rejecting the load disturbance and the constraint becomes inactive.

5.2 RC and RL Load

Fig. 6 shows the waveforms of the integrated EV drive with the proposed control structure with RC and RL load types. At $t = 0ms$, an RC type load with impedance $Z = 10 - 3.18j\Omega$ is connected across the output. It can be seen in Fig. 6(a) that the output voltage v_o is successfully tracking its sinusoidal reference v_{ref} . Moreover, as shown in Fig. 6(b), the current zero crossing is preceding the zero crossing of the output voltage, hence signifying a capacitive dominant load. At $t = 45ms$, the load changes from capacitive to RL with a net impedance of $Z = 8.5 + 3.14j\Omega$. It is evident in Fig. 6(d) that the control input brings the output voltage back to the desired reference within $2.5ms$. It is also important to notice that control input successfully fulfils its stipulated operational constraints. Fig. 6(c) shows the inductor currents i_1 and i_2 whose difference is equal to the output current i_o . It is worthwhile to mention here that the load disturbance is introduced at

6. CONCLUSION

In this paper, a detailed modelling process for V2H mode of an SRM integrated electric vehicle drive has been addressed. Then a disturbance observer based, fixed switching frequency, constrained control mechanism for the same has been developed. It has been shown through several results that the proposed control achieves excellent reference tracking and disturbance rejection both in case of linear and non-linear loads and also successfully handles the system constraints with anti-windup mechanism. As a future work, it is of significant interest to develop the model and control for three-phase inverter for the subject integrated SRM drive.

REFERENCES

- Bayat, P., Baghrmian, A., and Bayat, P. (2018). Implementation of hybrid electric vehicle energy management system for two input power sources. *Journal of Energy Storage*, 17, 423–440.
- Gan, C., Wu, J., Hu, Y., Yang, S., Cao, W., and Guerrero, J.M. (2016). New integrated multilevel converter for switched reluctance motor drives in plug-in hybrid electric vehicles with flexible energy conversion. *IEEE Transactions on Power Electronics*, 32(5), 3754–3766.
- Hu, K.W., Yi, P.H., and Liaw, C.M. (2015). An ev srm drive powered by battery/supercapacitor with g2v and v2h/v2g capabilities. *IEEE transactions on industrial electronics*, 62(8), 4714–4727.
- Rassaei, F., Soh, W.S., and Chua, K.C. (2015). Demand response for residential electric vehicles with random usage patterns in smart grids. *IEEE Transactions on Sustainable Energy*, 6(4), 1367–1376.
- Robledo, C.B., Oldenbroek, V., Abbruzzese, F., and van Wijk, A.J. (2018). Integrating a hydrogen fuel cell electric vehicle with vehicle-to-grid technology, photovoltaic power and a residential building. *Applied energy*, 215, 615–629.
- Romo, R. and Micheloud, O. (2015). Power quality of actual grids with plug-in electric vehicles in presence of renewables and micro-grids. *Renewable and Sustainable Energy Reviews*, 46, 189–200.
- Saeed, J., Niakinezhad, M., Wang, L., and Fernando, N. (2019). An integrated charger with hybrid power source using pv array for ev application. In *2019 IEEE 13th International Conference on Compatibility, Power Electronics and Power Engineering (CPE-POWERENG)*, 1–6. IEEE.
- Sun, J., Mitchell, D.M., Greuel, M.F., Krein, P.T., and Bass, R.M. (2001). Averaged modeling of pwm converters operating in discontinuous conduction mode. *IEEE Transactions on power electronics*, 16(4), 482–492.
- Sun, Q., Wu, J., Gan, C., Si, J., Guo, J., and Hu, Y. (2019). Cascaded multiport converter for srm-based hybrid electrical vehicle applications. *IEEE Transactions on Power Electronics*.
- Wang, L. (2019). *Control Systems Design and Implementation using MATLAB®/Simulink®*. Wiley.
- Yan, J., Menghwar, M., Asghar, E., Panjwani, M.K., and Liu, Y. (2019). Real-time energy management for a smart-community microgrid with battery swapping and renewables. *Applied energy*, 238, 180–194.

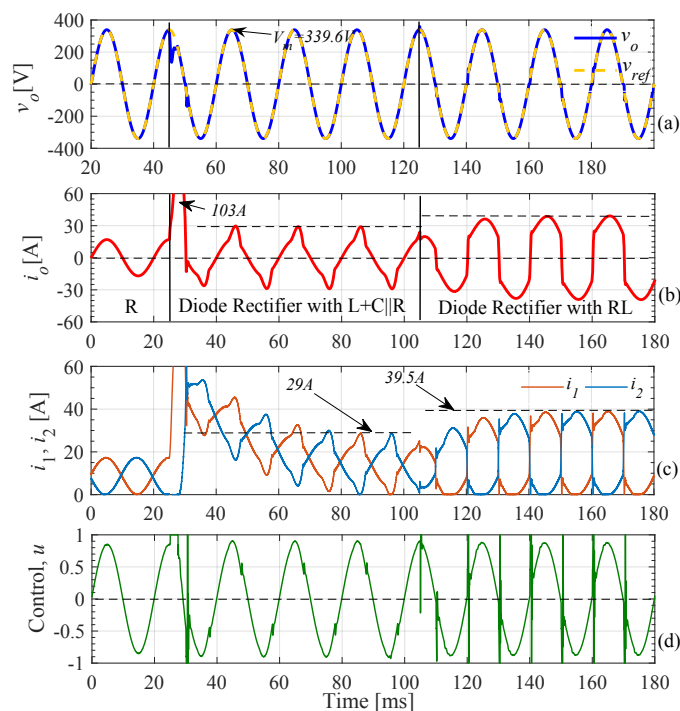


Fig. 7. Waveforms of standalone V2H mode with the proposed control in case of non-linear load. (a) Output voltage v_o . (b) Output current i_o . (c) Inductor currents, i_1 and i_2 . (d) Control input u .

the positive peak of the output voltage so as to analyse the worst case transience in the system output. If it was on a zero crossing or an off-peak value, the transience in the voltage would have been smaller.

5.3 Diode Rectifier Non-linear Load

In order to test the performance of the proposed control in presence of nonlinear load disturbance, a full-wave diode rectifier with multiple load types is connected across the output capacitor. The waveforms in Fig. 7(a) and 7(b) show the voltage and current in this case, respectively. At $t = 25ms$, the inverter load is changed from purely resistive to a diode rectifier with an LC filter and R load. It can be seen in Fig. 7(b) that a huge inrush current flows into the capacitor of LC filter that causes a dip in the output voltage. However, v_o recovers to its desired reference in less than $5ms$. Fig. 7(c) shows the control input which appears to be smooth from $t = 25$ to $105ms$. At $t = 105ms$, the load is changed to a diode rectifier with RL output. A large inductive load essentially draws a square-shaped current which is discontinuous at zero crossings. In this case, because of the hard commutation of the load current in every half cycle, the output voltage momentarily deviates from its reference at zero crossing. Consequently, the control signal exhibits fast changes at zero crossings to mitigate this, but it still remains within the specified operational bounds. It is important to note that despite the non-linear load, the proposed controller keeps the output voltage at its desired reference while exhibiting excellent disturbance rejection.